HHS Public Access

Author manuscript

Nat Nanotechnol. Author manuscript; available in PMC 2017 December 19.

Published in final edited form as:

Nat Nanotechnol. 2017 August ; 12(8): 821–829. doi:10.1038/nnano.2017.109.

Sulfated Glycopeptide Nanostructures for Multipotent Protein Activation

Sungsoo S. Lee[1,2,8,†], **Timmy Fyrner**[1,†], **Feng Chen**[1], **Zaida Álvarez**[1], **Eduard Sleep**[1], **Danielle S. Chun**[3], **Joseph A. Weiner**[3], **Ralph W. Cook**[3], **Ryan D. Freshman**[3], **Michael S. Schallmo**[3], **Karina M. Katchko**[3], **Andrew D. Schneider**[3], **Justin T. Smith**[3], **Chawon Yun**[3], **Gurmit Singh**[3], **Sohaib Z. Hashmi**[3], **Mark T. McClendon**[1], **Zhilin Yu**[1], **Stuart R. Stock**[4], **Wellington K. Hsu**[1,3], **Erin L. Hsu**[1,3], and **Samuel I. Stupp**[1,2,5,6,7,*]

[1]Simpson Querrey Institute for BioNanotechnology, Northwestern University, Chicago, Illinois 60611, USA

[2]Department of Materials Science and Engineering, Northwestern University, Evanston, Illinois 60208, USA

[3]Department of Orthopaedic Surgery, Northwestern University, Chicago, Illinois 60208, USA

[4]Department of Molecular Pharmacology and Biological Chemistry, Northwestern University, Chicago, Illinois 60611, USA

[5]Department of Biomedical Engineering, Northwestern University, Evanston, Illinois 60208, USA

[6]Department of Chemistry, Northwestern University, Evanston, Illinois 60208, USA

[7]Department of Medicine, Northwestern University, Chicago, Illinois 60611, USA

Abstract

Biological systems have evolved to utilize numerous proteins with capacity to bind polysaccharides for the purpose of optimizing their function. A well-known subset of these proteins with binding domains for the highly diverse sulfated polysaccharides are important growth factors involved in biological development and tissue repair. We report here on supramolecular sulfated glycopeptide nanostructures, which display a trisulfated monosaccharide

*Corresponding author: s-stupp@northwestern.edu.

[8]Current address: Blau Laboratory, Baxter Laboratory for Stem Cell Biology, Stanford University School of Medicine, Stanford, California 94305, USA.

†These authors contributed equally to this work.

Author contributions

S.S.L., T.F., and S.I.S. conceived the project. S.S.L., T.F., E.S., and Z.A. designed and performed experiments and analyzed data. F.C., Z.A., D.S.C., J.A.W., R.W.C., R.D.F., M.S.S., K.M.K, A.D.S., J.T.S., C.Y., G.S., S.Z.H., M.T.M, and S.R.S. performed experiments. Z.Y. assisted in synthesis. S.R.S. W.K.H., and E.L.H. supervised the in vivo study and analysis. S.S.L., T.F., E.L.H., and S.I.S. wrote the manuscript. All authors accepted the final version of the manuscript.

Additional information

Supplementary information is available in the online version of the paper. Reprints and permissions information is available online at www.nature.com/reprints. Correspondence and requests for materials should be addressed to S.I.S.

Competing financial interests

A patent application that covers the technology described in this paper has been filed (PCT/US2016/027292).

on their surfaces and bind five critical proteins with very different polysaccharide binding domains. Binding does not disrupt the filamentous shape of the nanostructures or their internal β-sheet backbone, but must involve accessible adaptive configurations to interact with such different proteins. The glycopeptide nanostructures amplified signaling of bone morphogenetic protein 2 significantly more than the natural sulfated polysaccharide heparin, and promoted regeneration of bone in the spine with a protein dose that is 100-fold lower than expected. These super-bioactive nanostructures may enable many therapies in the horizon involving proteins.

Glycans and proteins are important molecular partners in many functions of biological systems, commonly taking the form of covalent glycosylation of proteins or their noncovalent binding by polysaccharides[1–3]. Mapping all functions involved is a field in progress, but clearly glycans do play a role in potentiating cell signaling by proteins and protecting them from enzymatic degradation[4–7]. In this context, nanostructures that incorporate glycan and peptide chemistry could be key enablers of novel protein therapies in the horizon by activating function and protecting structure of proteins through programmed interactions. Glycosaminoglycans (GAGs) are heterogeneous polysaccharides ubiquitously found in mammalian tissues, and heparan sulfate (HS) is a highly sulfated GAG with enormous structural diversity known to interact with a plethora of proteins to regulate many physiological processes[1,8,9]. For this reason, the dominant HS saccharide structures are a great choice to develop a platform of glycopeptide nanotechnology. In fact, more than 300 secreted or membrane bound proteins have been found to bind HS and their biological functions are associated with a broad range of phenomena including cell differentiation, morphogenesis and organogenesis during development, blood coagulation, lipid metabolism, inflammation, and response to injury, among many others. The proteins known to interact with HS include growth factors (GFs), chemokines, enzymes, enzyme inhibitors, extracellular matrix proteins, and membrane bound receptors. HS is known to potentiate key GFs responsible for cell proliferation and differentiation, including bone morphogenetic protein (BMP)-2 which is important in bone formation[4], as well as vascular endothelial growth factor (VEGF) and fibroblast growth factor (FGF) which mediate the formation of blood vessels[1].

The use of HS as a therapy to potentiate bioactivity of proteins has been hindered by its limited availability and its enormous chemical heterogeneity. The chemical heterogeneity of HS is put into perspective by the fact that a simple disaccharide in its sequence could have up to 48 possible structures[10], and this biopolymer has molecular weights in the range of 20–100 kDa[1]. A close analog of HS is the biopolymer heparin with a more homogeneous structure than HS and lower molecular weights. Heparin can be easily isolated and is also known to potentiate some of the HS binding GFs[4,8,11]. However, heparin is a well-known anticoagulant in clinical use and this has been an obstacle to its broader application as a bioactive therapy. This has inspired the development of fractionated HS chains with specific protein affinities[12], synthetic heparin variants[13], as well as mimetic systems of linear glycopolymers and branched glycodendrimers[14–17]. In this work we have developed glycopeptide supramolecular nanostructures displaying on their surfaces a dominant molecular motif of sulfated polysaccharides, and demonstrated their ability to bind and activate multiple proteins as well as their potential to remain bioactive *in vivo*.

Design of supramolecular glycopeptide nanostructures

The key molecular design feature in the supramolecular nanostructures was the use of sulfated monosaccharides given that sulfation is the structural hallmark of the natural polysaccharides' ability to bind hundreds of proteins in biology[1]. These moieties (as well as others that are carboxylated rather than sulfated or charge neutral) are placed at the terminus of peptide amphiphiles (PAs) with a strong tendency to form β-sheets, well-known to form nanoscale filaments that mimic extracellular matrix components[18,19]. Thus, supramolecular self-assembly displays the monosaccharides on the surface of the 1D nanostructures (synthetic procedures for the monosaccharides are described in supplementary information). Previous supramolecular systems did not incorporate sulfated monosaccharides and either linked readily available simple sugars directly to amino acids or to synthetic aromatic units via a spacer[20–23]. Heparin and HS are rich in both *N*-sulfated glucosamine (GlcNS) and sulfated L-iduronic acid (IdoA2S) residues[1]. However, we designed our glycopeptides using *N*-acetyl glucosamine (GlcNAc) based monosaccharides motivated by the potential scalability of our nanostructures for clinical translation. In this context we focused on the possibility that supramolecular presentation of sulfated GlcNAc monosaccharides, and their associated water molecules, could interact at least with certain HS binding growth factors.

PAs were glycoconjugated via copper(I)-catalyzed alkyne-azide cycloaddition (CuAAC)[24] with a series of azido functionalized monosaccharides: trisulfated 3,4,6S-*N*-acetyl glucosamine (3,4,6S-GlcNAc) (PA **1**), monosulfated 6S-GlcNAc (PA **2**), monocarboxylated glucuronic acid (GlcA) (PA **3**), and uncharged GlcNAc (PA **4**) (Fig. 1a, and Supplementary Fig. 1). The Cu catalyst was removed from synthesized molecules, leaving only trace amounts of Cu (~21 ppb) which is lower than the average concentration in blood (1.1 ppm)[25]. This molecular design separates the monosaccharide from the peptide sequence by a short spacer to facilitate surface display on the nanostructure. A representative cryogenic transmission electron micrograph (cryo-TEM) revealed the self-assembly of the glycopeptide amphiphiles (GPAs) into nanoscale filaments at concentrations of 25 μM (Fig. 1b, and Supplementary Fig. 2). Small-angle X-ray scattering (SAXS) profiles from PAs **1–6** exhibited a slope of −1 in the low-q range (Fig. 1c), which is indicative of the formation of high aspect ratio filaments in solution[26]. Also, the scattering minima in the range of $q = 0.06$ to 0.07 $Å^{-1}$ correspond to diameters of 8.9 to 10.5 nm, comparable to those observed in cryo-TEM images. The formation of these filaments is well-known to involve hydrophobic collapse of aliphatic tails and β-sheet formation[27,28] among peptide segments (Supplementary Fig. 3). Zeta potential measurements revealed that trisulfated PA **1** exhibited the highest net negative charge relative to PAs **2–4** (Fig. 1d), indicating that the monosaccharides are exposed on the surface of the nanostructures.

Protein binding by glycopeptide nanostructures

Using surface plasmon resonance (SPR) spectroscopy, we evaluated the binding capacity of the glycopeptide nanostructures to seven biologically important heparin binding GFs (BMP-2, BMP-4, FGF-1, FGF-2, VEGF, Sonic hedgehog (Shh)) and one GF inhibitor (noggin) (Fig. 2a). Proteins were covalently immobilized on an alginate surface, and the glycosylated PAs and other control analytes were injected to measure binding. Since

sulfation of heparin is crucial for its interaction with proteins[1], we compared the protein-binding behavior of heparin and nanostructures comprised of trisulfated PA **1**. Heparin (0.01–100 μM) exhibited a strong concentration-dependent binding to six of the seven proteins, with the exception of noggin. PA **1** nanofibres (10–60 μM) bound to five proteins, excluding Shh and noggin (Fig. 2b).

Equilibrium dissociation constants (K_D) between heparin and the proteins were calculated from the SPR data. However, one mole of heparin has many more monosaccharide moieties than one mole of PA, and therefore the calculated binding constants from the SPR data are significantly underestimated for the supramolecular nanostructures. The values obtained are therefore only useful for comparative purposes among the various supramolecular nanostructures (Fig. 2c, and Supplementary Fig. 4). We did not observe a strong binding to noggin from either heparin or PA **1**, despite the fact that noggin has a heparin binding domain[29]. This could be due to an inherent issue with the SPR setup, in which proteins have to be covalently bound to the substrate, and it is therefore possible that binding domains are not necessarily displayed to heparin or PA nanofibres. Interestingly, PA **4** nanofibres (10–60 μM) exhibited negligible binding to all of the proteins (Fig. 2b), which suggests that the high degree of sulfation in the monosaccharides is critical to the strong binding observed by PA **1**. We also found that the azide-derivative of trisulfated monosaccharide **1** (10–60 μM) which is not programmed for self-assembly does not bind to any of the proteins, highlighting the importance of multivalent interactions[30] afforded by supramolecular aggregates of PA **1.** In fact, the SAXS curve of the monosaccharide solution is identical to that of the dissolving buffer, demonstrating the absence of any significant supramolecular structure (Supplementary Fig. 5).

We also investigated the interactions between glycopeptide nanoscale filaments and a heparin binding protein using confocal fluorescence imaging. For visualization, we co-assembled PAs **1** or **4** with a small fraction of PA molecules labeled with a fluorescent cyanine dye (Cy3-PA, 5 mol%), and BMP-2 as a model protein was fluorescently labeled with a different cyanine dye (Cy5). PA nanostructures and BMP-2 were allowed to mix for 24 h before imaging. Interestingly, confocal microscopy revealed a strong colocalization of BMP-2 along the fibrous nanostructures of trisulfated PA **1** (Fig. 2d, top), and in great contrast BMP-2 did not localize with nonsulfated PA **4** nanofibres (Fig. 2d, bottom) (colocalization was not observed between PA **1** nanofibres and free Cy5 dyes; Supplementary Fig. 6). To further eliminate any potential artifacts from dye-dye interactions, we also mixed fluorescently labeled BMP-2 with non-fluorescent PA nanostructures, and clearly observed filamentous profiles (Supplementary Fig. 6).

Structural stability of glycopeptide nanostructures

SAXS was performed to measure the influence of protein binding on glycopeptide self-assembly. Upon mixing with the proteins, we did not observe any change in the X-ray scattering of glycopeptide nanostructures (Fig. 3a, and Supplementary Fig. 7). Proteins alone did not scatter X-rays, and hence we suggest that the binding of proteins does not disrupt the filamentous morphology. Also, circular dichroism (CD) measurements revealed that the β-sheet secondary structure of the glycopeptide nanofibres remained unperturbed by the

addition of the heparin binding proteins (Fig. 3b). Although the monomeric units are connected by noncovalent interactions, this binding substrate remained structurally invariant upon binding proteins. The findings here suggest that protein binding likely occurs at the glycosylated surface or hydrated spaces of the nanofibres and that the assemblies are architecturally stable as they associate with different proteins. Maintaining the structural integrity of the biomimetic nanofibres is important since dimensional changes can drastically change their interactions with cells[31].

Regulation of protein activity

We investigated if the glycopeptide nanostructures could emulate the ability of heparin to regulate BMP signaling. We selected BMP-2 as a model GF since heparin and HS can enhance BMP-2 signaling by prolonging its bioavailability and inhibiting its antagonist noggin[4,5,12]. For this purpose, we used C2C12 mouse myoblasts, a well-known cell line for which differentiation into osteoblasts occurs upon exposure to BMP-2[32]. Cells were cultured with BMP-2 (75 ng/mL) in the presence of heparin, HS, or glycopeptide filaments for 3 days, and osteoblast differentiation was evaluated by monitoring expression of the osteogenic protein alkaline phosphatase (ALP) (Fig. 4a). We observed a dose response increase in osteoblast differentiation by both heparin and HS (Supplementary Fig. 8), but in agreement to previous work heparin exhibited a more potent response than HS[4]. HS was found to enhance the level of ALP expression by a factor of 3 and heparin by a factor of 5. As discussed below, we found that the sulfated glycopeptide nanostructures revealed in this assay a level of ALP expression that was 9 times higher than BMP-2 alone.

Upon exposure to the glycopeptide nanostructures (25 μM), the augmentation of BMP-2 activity strongly depended on the nature of the monosaccharide and its density on nanostructure surfaces. A series of glycopeptide nanostructures was evaluated by co-assembling PAs **1–4** with the non-glycosylated PA **6** (these assemblies all revealed the formation of similar nanoscale filaments, Supplementary Fig. 9). PA **6** alone (0% monosaccharide density) resulted in a 5-fold increase in ALP activity (Fig. 4a), likely due to non-specific, coulombic interactions between the acidic nanofilaments and basic BMP-2[33]. In contrast, ALP activity was found not to be enhanced when PA **3** or **4** were incorporated at the level of 10% or higher. We believe these results suggest that nanofibres formed by these co-assemblies exhibit non-fouling behavior towards proteins and cells. This phenomenon is well-known in the context of epithelial cell membranes and bacteria, which display similar behavior as a result of their glycocalyx[34]. In fact, inspired by the glycocalyx, synthetic non-fouling surfaces have been developed using nonionic oligosaccharides or poly(ethylene glycol)[35–37]. To support this suggestion, we co-assembled PA **5**, which is end-functionalized with oligo(ethylene glycol), with PA **6** and found as expected a negligible effect on the enhancement of BMP-2 activity (Supplementary Fig. 10). Furthermore, zeta potential measurements revealed that the presence of GlcNAc and oligo(ethylene glycol) (PAs **4**, **5**) indeed screened the net negative charge on nanostructure surfaces compared to those formed by PA **6** (Fig. 1d).

Glycopeptide nanofilaments containing negatively charged glucuronic acid moieties (PA **3**) were found not to potentiate BMP-2 activity (Fig. 4a). In the case of nanofibres containing a

monosulfated monosaccharide (PA **2**), we did observe a 3-fold increase in BMP-2 signaling. These two negatively charged PA nanostructures have comparable zeta potentials (Fig. 1d) and their aqueous solutions exhibit effectively identical changes in pH when HCl is titrated (Supplementary Fig. 11). Therefore this observation cannot be simply explained by charge density differences. On the other hand, sulfates are known to form stronger salt bridges with the side chains of lysine and arginine relative to carboxylates[38]. Since lysine and arginine are common amino acids in the heparin binding domains of proteins, this difference between carboxylates and sulfates could very well explain our results with PA **3** versus PA **2**. In addition, the increase in BMP-2 induced ALP activity by PA **2** nanostructures was less than those formed by PA **6**. Although PA **6** was not glycosylated, the presentation of glutamic acid residues on the surface of the supramolecular assemblies led to a greater negative zeta potential than that of PA **2** assemblies (Fig. 1d). Thus, nanostructures that are more acidic can likely bind nonspecifically to cationic proteins and alter their bioactivities. Interestingly, glycopeptide nanostructures containing the trisulfated monosaccharide 3,4,6S-GlcNAc (PA **1**) dramatically amplified BMP-2 signaling (Fig. 4a, and Supplementary Fig. 12). At 100% monosaccharide density, PA **1** nanostructures enhanced ALP activity by 9-fold, significantly higher than other glycosylated nanostructures, non-glycosylated PA **6** nanostructures, or the naturally occurring sulfated polysaccharides, heparin and heparan sulfate. The high charge on PA **1** nanostructures revealed by zeta potential measurements (Fig. 1d) is likely to be part of the stronger interaction between these supramolecular assemblies and BMP-2. We also found that PA **1** filaments promoted higher expressions of *ALP* and osteocalcin (*OCN*) mRNA relative to heparin (0.62 μM or 10 μg/mL) or the PA nanostructures displaying uncharged GlcNAc residues (Fig. 4b).

In the SPR analyses (see Fig. 2b), the azide-derivative of trisulfated monosaccharide **1** was found to bind neither BMP-2 nor BMP-4, another osteogenic heparin binding GF similar to BMP-2[5]. We therefore tested here if monosaccharide **1** amplified BMP-2 and BMP-4 signaling in C2C12 cells and in fact found this not to be the case (Fig. 4c). Also, heparin and HS are known to prolong the half-life of BMP-2[4,5], and indeed we observed improved BMP-2 stability in cell culture media in the presence of heparin or PA **1** nanostructures, but not in the presence of monosaccharide **1** (Supplementary Fig. 13). Our experiments suggest that the collective interactions afforded by supramolecular nanostructures of PA **1** are necessary to bind GFs and regulate their bioactivity.

Next, we sought to compare the influence of two different glycopeptide nanofibres that present the same number of sulfates (hence identical ionic strength), but with different sulfation patterns. The first nanofibre system was comprised entirely of monosulfated PA **2**, whereas the second system was comprised of trisulfated PA **1** and nonsulfated PA **4** at a 1:2 molar ratio. Interestingly, these two nanofibres (25 μM) exhibited significantly different effects on BMP-2 (75 ng/mL) induced ALP expressions in C2C12 cells (Fig. 4d). This suggests that the pattern of the charged groups is important and that the nanofibre-growth factor binding is not exclusively based on nonspecific electrostatic interactions. Furthermore, we investigated the binding mechanism of PA **1** nanostructures by using a mutant form of BMP-2 (EHBMP-2) that activates Smad phosphorylation to the same degree as the wild type BMP-2 while possessing negligible binding affinity to heparin[39,40]. Previous work showed

that wild type BMP-2 signaling is definitely affected by the removal of cell surface HS by heparitinase, but the mutant protein EHBMP-2 remains unaffected by the absence of HS[40]. Interestingly, we found that the mutation of BMP-2's heparin binding domain minimized the effect of PA **1** nanofibres. While the amplification of wild type BMP-2 signaling was greater with PA **1** nanofibres than that with heparin or the non-glycosylated PA **6** nanofibres (see Fig. 4a), the amplification of EHBMP-2 signaling with PA **1** nanostructures was marginal and rather comparable to that with heparin or PA **6** nanofibres (Fig. 4e). This observation supports the hypothesis that the sulfated glycomimetic nanostructures interact with the heparin binding pocket of wild type BMP-2.

Sulfated polysaccharides also regulate noggin[5,41]. While noggin antagonizes BMPs, heparin binds and inhibits noggin activity, thereby rescuing BMP signaling and the subsequent ALP expression in C2C12 cells. Interestingly, exposure to PA **1** nanoscale filaments also successfully protected BMP-2 from noggin antagonist (50 ng/mL) during osteoblast differentiation and still yielded ALP activity that is higher than that with BMP-2 alone without noggin (Fig. 4f). In addition, the long term effect of the glycopeptide nanofibres on matrix mineralization of C2C12 cells was assessed by Alizarin Red S staining after 10 days of culture (Fig. 4g,h). Heparin (0.62 μM or 10 μg/mL) inhibited BMP-2 (100 ng/mL) dependent mineralization, and previous studies have shown similar findings and hypothesized that heparin could chelate Ca^{2+} ions and thereby lower its bioavailability for mineralization[4,42]. In contrast, BMP-2 combined with PA **1** nanofibres (25 μM) rather enhanced matrix mineralization relative to the GF alone, while other control nanostructures showed minimal effects (Fig. 4h).

We also assessed whether the influence of the glycopeptide nanostructures on osteogenic differentiation occurred specifically through the BMP signal transduction pathway. BMP ligands activate BMP receptors, which subsequently phosphorylate intracellular SMAD transcription factors for downstream gene transcription[43]. Hence, C2C12 cells were stimulated with various conditions, then lysed and immunoblotted to detect the levels of pSmad1/5 (Fig. 4i,j). In the absence of BMP-2, treatment with heparin (0.62 μM) or PA **1** nanofibres (25 μM) did not enhance accumulation of pSmad proteins, suggesting that BMP-2 ligand is required to initiate signaling (see Fig. 4a–h). When cultured with the combination of BMP-2 (75 ng/mL) and heparin or PA **1** nanofibres for 3 h, the mean values of normalized pSmad protein accumulation was found to be significantly higher relative to that with BMP-2 alone. Also, the addition of a selective inhibitor of BMP type I receptor kinases[43], LDN-193189 (0.5 μM), impeded the BMP-2 mediated phosphorylation of Smads, regardless of the presence of heparin or PA **1** nanofibres. Theses results demonstrate that the combination of the trisulfated glycopeptide nanostructures and BMP-2 successfully activates intracellular events associated with BMP signaling pathway.

We also investigated the influence of the glycopeptide nanostructures on FGF signaling using BaF3-FR1C cells, which lack cell membrane HSGAGs and thus require exogenous heparin or HS to promote FGF-receptor (FGFR) interaction[11]. While heparin exhibited a concentration-dependent amplification of FGF-2 (1 ng/mL) mediated proliferation of BaF3-FR1C cells, we did not observe a strong enhancement of FGF-2 activity by the glycopeptide nanostructures (Supplementary Fig. 14). The formation of a ternary FGF-FGFR-HS

complex is known to be crucial for active FGF signaling[44]. Hence, we speculate that even though the trisulfated PA **1** nanofibres exhibit strong affinity to FGF-2 (see Fig. 2b–c), the nanostructure does not have the appropriate architectural configuration or dimensions to form the necessary ternary complex for FGF-2 activation in this *in vitro* assay. However, the binding of this angiogenic GF by PA 1 nanofibres may still be therapeutically useful *in vivo* through its protection from enzymatic degradation, an issue beyond the scope of this paper.

Bone regeneration *in vivo*

We investigated the translational potential of the supramolecular glycopeptide nanostructures. Ideal biomaterials for tissue regeneration should not be anticoagulant since hematoma formation is the first stage of wound repair[45]. By monitoring Factor Xa activity that is inhibited by heparin-activated antithrombin[46], we observed that the anticoagulant activity of PA **1** nanofibres towards Factor Xa was <0.01% of the activity of unfractionated heparin (Fig. 5a). This was expected since a highly specific pentasaccharide sequence in heparin is necessary for activating antithrombin[47], and we postulate that the presentation of 3,4,6S-GlcNAc monosaccharides in PA **1** assemblies simply cannot mimic the characteristic pentasaccharide to activate antithrombin. This is of course a major translational advantage of the PA1 nanostructures in the context of surgical interventions for bone regeneration.

We evaluated the glycopeptide assemblies in a well-established rat posterolateral lumbar intertransverse spinal fusion model, which historically requires 10 μg BMP-2 loaded on a collagen sponge for effective bilateral fusion between L4 and L5 transverse processes[33]. Animals were treated with a dose of BMP-2 that is 100 times lower than that required in the model (100 ng) in the presence or absence of the PA nanostructures (6 mM). A 10 μg BMP-2 dose was also assessed as a positive control. Eight weeks post-treatment, blind manual palpation analyses demonstrated that PA **1** nanostructures elicited the highest fusion scores relative to PA **4** and PA **6** nanostructures or saline (Fig. 5b). PA **1** nanostructures led to a 100% fusion rate using the very low sub-therapeutic dose of BMP-2 (Fig. 5c), thereby reducing the required GF by 100-fold. This observation suggests that bone regeneration efficacy by the glycopeptide nanostructures is not simply rooted in non-specific electrostatic interactions with BMP-2. PA **1** nanofibres with an even lower dose of BMP-2 (10 ng) or none did not yield fusion (Supplementary Fig. 15). PA **6** nanofibres, which exhibited some limited bioactivity *in vitro* (see Fig. 4a), also did not yield fusion *in vivo* in the absence of exogenous BMP-2 (see Supplementary Fig. 15).

Quantitative analyses of micro-computed tomography (μCT) reconstructions revealed that in the presence of 100 ng BMP-2, PA **1** had by far the highest mean volume of new ossified tissue relative to other control treatments containing an equal dose of BMP-2 (Fig. 5d). This mean volume was lower than that that observed in animals treated with 10 μg BMP-2 alone (positive control), partially owing to multilevel fusions found in positive control animals as shown in Fig. 5e. However, high-resolution synchrotron X-ray μCT analysis of the fused spine from the 100 ng BMP-2 and PA **1** combination therapy revealed robust cortical shell throughout the fusion bed (Fig. 5f, and Supplementary Movie 1), suggesting that the sub-therapeutic dose of BMP-2 was in fact therapeutically adequate when combined with the trisulfated glycopeptide nanostructures. Finally, histological analyses of spine specimens,

using hematoxylin and eosin (H&E) stain, confirmed the results from μCT measurements (Fig. 5g). Treatment with PA **1** nanostructures in the presence of 100 ng BMP-2 demonstrated robust fusion mass, and no evidence of a local inflammatory response was found in any of the specimens. The 100-fold reduction in GF amount necessary for spinal fusion is of critical importance in the clinical use of BMP-2 due to the dangerous side effects that have been reported recently in patients[48].

Conclusions

We found that filamentous glycopeptide nanostructures exhibit great capacity to bind important GFs in development and tissue regeneration. The diverse nature of heparin binding domains suggests that the interactions involve more than non-specific electrostatics. Since proteins could penetrate the nanofibre's highly hydrated peptide shell[49,50], the supramolecular assemblies can display a large diversity of binding sites in their peptide sequences. These can in turn interact with heparin binding domains of proteins without disrupting their filamentous morphology or internal substructure of β-sheets. We hypothesize that the diversity of molecular environments adapting to optimize interactions with different proteins also benefits greatly from the liquid-like rotational diffusion known to exist on the surfaces of similar peptide supramolecular filaments[27]. Information on the exact binding environment for each protein would not be experimentally accessible at this time, but it is clear that the glycopeptide nanostructures are able to mimic heparin and HS to strongly influence biological signals *in vitro* and *in vivo*. With further discoveries on glycan interactions with proteins and advances in glycan synthesis, the class of supramolecular nanostructures described here could become great vehicles to deliver, activate, and protect proteins used as novel therapies for disease and regenerative medicine.

Methods

Methods and any associated references are available in the online version of the paper.

Methods

General methods for chemical synthesis and purification

Organic solvents where dried over $MgSO_4$ before concentration under reduced pressure at <40 °C (bath temperature). Thin layer chromatography (TLC) was carried out on Merck precoated silica gel 60 F_{254} plates with detection by UV light and/or charring with PAA [*p*-anisaldehyde (20 mL), acetic acid (100%, 8.4 mL), sulfuric acid (conc., 28 mL), ethanol (95%, 740 mL)], AMC [ammonium molybdate (10 g), cerium(IV)sulfate (2 g), sulfuric acid (10%, 200 mL)] or PMA [phosphomolybdic acid (7 g), ethanol (100 mL) followed by heating at ~250 °C. Flash column chromatography (FC) was carried out on Merck silica gel 60 (40–63 μm). Gradient preparative high-performance liquid chromatography (HPLC) was carried out on a Varian ProStar system (column: Phenomenex C-18, 250x30.0 mm, 5 μm; λ = 220 nm; Varian fraction collector model 701) using acetonitrile with 0.1 % NH_4OH and Milli-Q water with 0.1 % NH_4OH as mobile phases. High resolution mass spectra (HRMS) were recorded on an Agilent 6210A LC-TOF mass spectrometer in positive or negative ion mode. Maldi-TOF was performed on a Bruker Autoflex III using Sinapinic acid as a matrix.

ATR-IR spectra were acquired on a Bruker Tensor 37 FTIR spectrometer equipped with a Mid IR detector between 400 and 7000 cm^{-1} where appearances are quoted as strong, medium, and weak. Peptide content analysis was performed on the purified product (AIBiotech) to ensure concentration accuracy and consistency for all experiments.

LC-MS purity measurements

Analytical LC-MS was performed on an Agilent 1200 system (Column: Phenomenex C-18 150 x 5.00 mm, 5 μm). MS detector: Agilent 6520 Q-TOF/MS. Gradient: acetonitrile 5% for 5 min at 50 μL/min, 5–95% over 30 min at 50 μL/min followed by 95% for 5 min at μL/min. To all solvents ammonium hydroxide (0.1 % v/v) was added. Peaks were detected at 220 nm.

NMR spectroscopy

Proton nuclear magnetic resonance (^1H) were recorded on an Agilent 500 MHz DD2 or an Agilent 600 MHz DD2 w/HCN cryoprobe. Carbon nuclear magnetic resonance (^{13}C) were recorded on a Bruker AVANCE III 500 MHz w/direct cryoprobe or an Agilent 600 MHz DD2 w/HCN cryoprobe. NMR spectra were recorded at 25 °C using CD_3OD, D_2O, DMF-d_7, or DMSO-d_6 as solvents. Chemical shifts are reported in part per million (ppm) where tetramethylsilane (TMS), the solvent residual peaks or methanol (for D_2O) are used as internal standards [CDC_{l3} (^1H-NMR, δ = 7.26 ppm; ^{13}C-NMR, δ = 77.2 ppm), D_2O (^1H-NMR, δ = 3. 34 ppm; ^{13}C NMR, δ = 49.5 ppm), DMF-d_7 (^1H-NMR, δ = 8.03 ppm; ^{13}C-NMR, δ = 163.2 ppm)][51]. Structural assignment was performed using ^1H,^1H-gCOSY, ^1H,^{13}C-gHSCQAD and ^1H,^{13}C-gHMBCAD. Multiplicities are quoted as singlet (s), doublet (d), double of doublets (dd), double double of doublets (ddd), triplet (t), apparent doublet (ad), apparent double of doublets (add), apparent triplet (at), quartet (q).

Peptide synthesis

See Scheme S1. Peptides where synthesized on solid support using Rink amide MBHA resin (100–200 mesh, 0.59 meq/g) with Fmoc-based procedures. A Lys(Mtt) was incorporated at selected position to enable orthogonal conjugation. Fmoc-NH-OEG_2-CH_2COOH (PurePEG) and 4-pentynoic acid (SigmaAldrich®) were used without further purification and HO-OEG_2-CH_2COOH was synthesized according to known procedure[52]. To a mixture of the amine (2 mmol, resin-bound), the acid (3 eq.), and DIPEA (4.5 eq.) in DMF (40 mL) was added HBTU (3 eq.). The reaction was performed in a reaction vessel for 1 h at room temperature when the beads where washed with CH_2Cl_2 (2x40 mL) and DMF (2x40 mL).

Fmoc deprotection

4-methylpiperidine (20% in DMF) was added (2x30mL) and the mixture was shaked for 10 mins at room temperature and washed with DMF (2x40 mL) and CH_2Cl_2 (2x40 mL).

N-methyltrityl (Mtt) deprotection

A mixture of freshly prepared TFA/TIS/CH_2Cl_2 (2:5:93) was added (2x30mL) to the resin-bound peptide and shaked for 1 h at room temperature and washed with DMF (2x40 mL) and CH_2Cl_2 (2x40 mL).

Cleavage from resin

The cleavage solution was prepared by mixing TFA/TIS/CH_2Cl_2 (2.5:2.5:95) and added (50 mL) to the resin-bound peptide, and the mixture was shaked for 1 h when the solution was collected and the resins where washed with additional CH_2Cl_2 (50 mL), evaporated and co-concentrated with toluene. The crude peptide was dissolved in 0.1 % NH_4OH (aq.), filtered using a 0.2 μm syringe filter and subjected to HPLC purification.

Click-reaction

The azido sugar (0.110 mmol) and Na-ascorbate (59.4 mg, 0.300 mmol) was added to a stirred solution of Alkyne PA (121 mg, 0.100 mmol) in DMF (4.00 mL) followed by the addition of 1M $CuSO_4$ (30.0 μL). The reaction mixture was stirred at room temperature for 1 h (monitored by direct-LC(Q)-TOF MS), diluted with H_2O (5.00 mL) and pH was adjusted with 30% (aq.) NH_4OH (50.0 μL). Chelex®-100 ion exchange resins (3x500 mg) was added and the slurry was stirred for 30 min, filtered and concentrated. The solution was subject to Chelex®-100 treatment until the bead no longer changed color (on average 3 times). HPLC followed by lyophilization gave the target PA in 24–57 % yield as a white solid.

2-Azidoethyl 2-acetamido -3,4,6-tri-O-sulfo-2-deoxy-β-D-glycopyranoside (monosaccharide 1)—To a solution of 2-Azidoethyl 2-acetamido-2-deoxy-β-D-glucopyranoside[53] (1.00 g, 3.45 mmol) in dry DMF (60.0 mL) Me_3NSO_3 (7.19 g, 51.7 mmol) was added and stirred overnight at 50°C. MeOH (10.0 mL) was added and the reaction mixture was stirred for 1 h at room temperature when the solution was evaporated and co-concentrated. FC (MeCN/H_2O/NH_3 6:1:0.5) gave title compound monosaccharide **1** (1.62 g, 3.05 mmol, 89%) as a colorless solid. R_f = 0.36 (MeCN/H_2O/NH_3 6:1:0.5); ATR-IR $\nu_{max}cm^{-1}$: 3197 (strong, broad), 3070 (strong, broad), 2110 (medium) 1633 (medium), 1565 (medium), 1423 (strong), 1161 (strong), 1039 (strong), 793 (strong); ^{13}C-NMR (100 MHz, D_2O): δ = 22.3 ($\underline{C}H_3$), 50.3 ($OCH_2\underline{C}H_2N$), 54.4 (C-5), 67.5 (C-6), 69.2 ($O\underline{C}H_2CH_2N$), 72.5 (C-2), 74.4 (C-4), 78.3 (C-3), 100.4 (C-1), 174.7 ($CH_3\underline{C}O$); ^{1}H-NMR (500 MHz, D_2O): δ = 2.01 (s, 3H, $C\underline{H}_3$), 3.46 (1H, ddd, *J* = 3.0, 5.6, 13.8 Hz, $OCH_2C\underline{H}_2N$), 3.57 (ddd, 1H, *J* = 3.0, 7.8, 13.8 Hz, $OCH_2C\underline{H}_2N$), 3.87 (ddd, 1H, *J* = 3.0, 7.8, 11.4 Hz, $OC\underline{H}_2CH_2N$), 3.97–4.02 (m, 2H, H-2, H-5), 4.12 (ddd, 1H, *J* = 3.0, 5.6, 11.4 Hz, $OC\underline{H}_2CH_2N$), 4.19 (dd, 1H, *J* = 7.8, 11.5 Hz, H-6a), 4.31 (dd, 1H, *J* = 8.9, 9.7 Hz, H-4), 4.56 (dd, 1H, *J* = 8.9, 10.2 Hz, H-3), 4.64 (d, 1H, *J* = 2.3, 11.5 Hz, H-6b), 4.79 (d, 1H, *J* = 8.1 Hz, H-1); HRMS-ESI [M – H]: calcd for $C_{10}H_{18}N_4O_{15}S_3$, 528.9853; found, 528.9850.

2-Azidoethyl 2-acetamido-6-O-sulfo-2-deoxy-β-D-glucopyranoside (monosaccharide 2)—2-Azidoethyl 2-acetamido-2-deoxy-β-D-glucopyranoside[53] (0.50 g, 1.72 mmol) was dissolved in dry DMF (20.0 mL) whereupon Me_3NSO_3 (1.20 g, 8.61 mmol) was added and the solution was stirred at 50 °C. After 2 h, the solution quenched with MeOH (10.0 mL) and solution was stirred at room temperature for 1 h when the mixture was evaporated and co-concentrated. FC (MeCN/H_2O/NH_3 6:1:0.5) gave title compound monosaccharide **2** (0.53 g, 1.42 mmol, 83%) as a colorless solid. R_f = 0.49 (MeCN/H_2O/NH_3 6:1:0.5); ATR-IR $\nu_{max}cm^{-1}$: 3189 (strong, broad), 3095 (strong, broad), 2107 (strong), 1633 (medium), 1560 (medium), 1430 (strong), 1197 (strong), 1056 (medium), 991 (strong), 759 (strong); ^{13}C-NMR (100 MHz, D_2O): δ = 22.3 ($\underline{C}H_3CO$), 50.3

($OCH_2\underline{C}H_2N$), 55.4 (C-2), 67.0 (C-6), 68.9 ($O\underline{C}H_2CH_2N$), 69.9 (C-4), 73.0 (C-5, C-3,), 101.1 (C-1), 174.6 ($CH_3\underline{C}O$); ^{1}H-NMR (500 MHz, D_2O): δ 2.11 (s, 3H, $C\underline{H}_3$), 3.49 (ddd, 1H, *J* = 3.0, 5.5, 13.7 Hz, $OCH_2C\underline{H}_2N$), 3.53–3.57 (m, 1H, $OCH_2C\underline{H}_2N$), 3.59 (at, 1H, *J* = 9.3 Hz, H-4), 3.64 (at, 1H, *J* = 9.4 Hz, H-3), 3.75 (m, 1H, H-5), 3.79–3.87 (m, 2H, H-2, $OC\underline{H}_2CH_2N$, overlap with residual $MeOSO_3H$), 4.11 (ddd, 1H, *J* = 3.0, 5.5, 11.4,Hz, $OC\underline{H}_2CH_2N$), 4.31 (add, 1H, *J* = 5.2, 11.2 Hz, H-6b), 4.42 (add, 1H, *J* = 1.9, 11.2 Hz, H-6a), 4.68 (d, 1H, *J* = 8.5 Hz, H-1); HRMS-ESI [M + H]: calcd for $C_{10}H_{18}N_4O_9S$, 371.0873; found, 371.0866.

3,4,6S-GlcNAc PA (PA 1)—PA **1** was prepared by conjugating Alkyne PA and monosaccharide **1** using general procedure for Click-reaction. ATR-IR $\nu_{max}cm^{-1}$: 3277 (strong, broad), 2919 (medium), 2850 (weak), 1627 (strong), 1543 (strong), 1399 (medium), 1227 (strong), 1020 (medium), 987 (weak); ^{13}C-NMR (125 MHz, DMF-d_7): δ 13.7 (Pal-CH_3), 16.2 (Ala-$\underline{C}_{(\beta)}H_3$), 17.6 (Ala-$\underline{C}_{(\beta)}H_3$), 18.0 (2xVal-$\underline{C}_{(\beta)}H_3$), 19.1 (Val-$\underline{C}_{(\beta)}H_3$), 19.3 (Val-$\underline{C}_{(\beta)}H_3$), 21.8 (triazolyl-$\underline{C}_{(\alpha)}H_2$), 22.5 (several Pal-$CH_2$), 22.6 (acetyl-$\underline{C}H_3$), 23.7 (Lys-$\underline{C}_{(\delta)}H_2$), 25.9 (Pal-$\underline{C}H_2$), 26.8 (Lys-$\underline{C}_{(\beta)}H_2$), 27.5 (Glu-$\underline{C}_{(\beta)}H_2$), 29.2 (Pal-$\underline{C}H_2$, overlaps with solvent peak), 29.2–29.9 (several Pal-$\underline{C}H_2$, overlaps with solvent peak), 30.5 (Val-$C_{(\gamma)}\underline{H}$), 30.5 (Val-$C_{(\gamma)}\underline{H}$), 30.9 (Glu-$\underline{C}_{(\gamma)}H_2$), 30.9 (Glu-$\underline{C}_{(\beta)}H_2$), 31.8 (several Pal-$\underline{C}H_2$), 34.2–35.8 (Glu-$\underline{C}_{(\gamma)}H_2$, Lys-$\underline{C}_{(\gamma)}H_2$, Pal-$\underline{C}_{(\alpha)}H_2$, overlaps with solvent peak), 35.2 (triazolyl-$\underline{C}_{(\beta)}H_2$), 38.5 (Lys-$\underline{C}_{(\varepsilon)}H_2$), 38.8 (OEG-$\underline{C}H_2$), 48.7 (Ala-$\underline{C}_{(\alpha)}H$), 49.8 ($OCH_2\underline{C}H_2N$), 50.8 (Ala-$\underline{C}_{(\alpha)}H$), 52.9 (Glu-$\underline{C}_{(\alpha)}H$), 53.6 (Glu-$\underline{C}_{(\alpha)}H$), 55.4 (C-2), 56.7 (Lys-$\underline{C}_{(\alpha)}H$), 58.5 (Val-$\underline{C}_{(\alpha)}H$), 58.7 (Val-$\underline{C}_{(\alpha)}H$), 67.6 (C-6), 67.6 ($O\underline{C}H_2CH_2N$), 69.4 (OEG-$\underline{C}H_2$), 69.8 (OEG-$\underline{C}H_2$), 70.3 (OEG-$\underline{C}_{(\alpha)}H_2$), 70.6 (OEG-$\underline{C}H_2$), 73.4 (C-4), 75.1 (C-5), 75.5 (C-3), 100.9 (C-1), 123.5 (triazolyl-$\underline{C}CH$), 146.3 (triazolyl-$\underline{C}H$), 170.0 ($\underline{C}O$), 170.6 ($\underline{C}O$), 171.3 ($\underline{C}O$), 172.1 ($\underline{C}O$), 172.5 ($\underline{C}O$), 172.7 ($\underline{C}O$), 173.5 ($\underline{C}O$), 173.8 ($\underline{C}O$), 173.9 ($\underline{C}O$), 175.0 ($\underline{C}O$), 175.0 ($\underline{C}O$), 178.0 ($\underline{C}O$), 178.0 ($\underline{C}O$); ^{1}H-NMR (600 MHz, DMF-d_7): δ 0.86 (t, 3H, *J* = 6.4 Hz, Pal-$C\underline{H}_3$), 0.90 (at, 12H, *J* = 6.9 Hz, Val-$C_{(\gamma)}\underline{H}_3$), 1.22–1.30 (m, 20H, Pal-$C\underline{H}_2$), 1.31–1.36 (m, 2H, Pal-$C\underline{H}_2$), 1.38 (d, 3H, *J* = 7.2 Hz, Ala-$C_{(\beta)}\underline{H}_3$), 1.43 (d, 3H, *J* = 7.3 Hz, Ala-$C_{(\beta)}\underline{H}_3$), 1.48–1.59 (m, 6H, Lys-$C_{(\delta)}\underline{H}_2$, Pal-$C\underline{H}_2$), 1.77–1.84 (m, 2H, Glu-$C_{(\beta)}\underline{H}_2$), 1.89 (s, 3H, acetyl-$C\underline{H}_3$), 1.89–1.92 (m, 2H, Glu-$C_{(\gamma)}\underline{H}_2$), 1.95–1.95 (m, 2H, Lys-$C_{(\beta)}\underline{H}_2$), 2.10–2.16 (m, 4H, Glu-$C_{(\beta)}\underline{H}_2$, Val-$C_{(\beta)}\underline{H}$, Val-$C_{(\beta)}\underline{H}$), 2.19–2.36 (m, 6H, Glu-$C_{(\gamma)}\underline{H}_2$, Lys-$C_{(\gamma)}\underline{H}_2$, Pal-$C_{(\alpha)}\underline{H}_2$), 2.60 (t, 2H, *J* = 7.9 Hz, triazolyl-$C_{(\beta)}\underline{H}_2$), 2.93–2.96 (m, 2H, triazolyl-$C_{(\alpha)}\underline{H}_2$), 3.17–3.23 (m, 2H, Lys-$C_{(\varepsilon)}\underline{H}_2$), 3.33 (t, 2H, *J* = 6.0 Hz, OEG-$C\underline{H}_2$), 3.50 (t, 2H, *J* = 6.0 Hz, OEG-$C\underline{H}_2$), 3.60–3.62 (m, 2H, OEG-$C\underline{H}_2$), 3.64–3.65 (m, 2H, OEG-$C\underline{H}_2$), 3.85–3.90 (m, 1H, H6b, overlaps with H_2O), 3.92–3.95 (m, 1H, Lys-$C_{(\alpha)}\underline{H}$, overlaps with H_2O), 3.96 (s, 2H, OEG-$C_{(\alpha)}\underline{H}_2$), 4.05–4.10 (m, 3H, H-2, H-5, Glu-$C_{(\alpha)}\underline{H}$), 4.15–4.22 (m, 4H, $OC\underline{H}_2CH_2N$, Ala-$C_{(\alpha)}\underline{H}$, Glu-$C_{(\alpha)}\underline{H}$), 4.30–4.34 (m, 3H, H-3, 2xVal-$C_{(\alpha)}\underline{H}$), 4.44 (dd, 1H, *J* = 2.6, 11.1 Hz, H6a), 4.51–4.55 (m, 2H, H-3, Ala-$C_{(\alpha)}\underline{H}$), 4.60–4.65 (m, 3H, H-1, $OCH_2C\underline{H}_2N$), 8.01 (s, 1H, triazole-$C\underline{H}$); HRMS-ESI [M – 2H]/2: calcd for $C_{69}H_{120}N_{14}O_{31}S_3$, 867.3625; found 867.3623; [Cu]: 6.00 ng/mg.

6S-GlcNAc PA (PA 2)—PA **2** was prepared by conjugating Alkyne PA and monosaccharide **2** using general procedure for Click-reaction. ATR-IR $\nu_{max}cm^{-1}$: 3276 (strong, broad), 2919 (medium), 2850 (weak), 1628 (strong), 1544 (weak), 1398 (medium), 1225 (strong), 1061 (medium), 1006 (medium); ^{13}C-NMR (125 MHz, DMF-d_7): δ 13.7

(Pal-CH$_3$), 16.7 (Ala-C$_{(\beta)}$H$_3$), 16.8 (Ala-C$_{(\beta)}$H$_3$), 18.2 (Val-C$_{(\gamma)}$H$_3$), 18.2 (Val-C$_{(\gamma)}$H$_3$), 19.0 (Val-C$_{(\gamma)}$H$_3$), 19.0 (Val-C$_{(\gamma)}$H$_3$), 21.7 (triazolyl-C$_{(\alpha)}$H$_2$), 22.5 (several Pal-CH$_2$), 22.5 (acetyl-CH$_3$), 23.3 (Pal-CH$_2$), 25.1 (Pal-CH$_2$), 26.7 (Glu-C$_{(\beta)}$H$_2$) 26.9 (Lys-C$_{(\gamma)}$H$_2$), 29.1 (Lys-C$_{(\delta)}$H$_2$), 29.1–29.8 (several Pal-CH$_2$, overlap with solvent peak), 30.0 (Val-C$_{(\beta)}$H), 30.0 (Val-C$_{(\beta)}$H), 30.8 (C$_{(\gamma)}$H$_2$/Lys-C$_{(\beta)}$H$_2$), 30.9 (C$_{(\gamma)}$H$_2$/Lys-C$_{(\beta)}$H$_2$), 30.9 (C$_{(\gamma)}$H$_2$/Lys-C$_{(\beta)}$H$_2$), 31.4 (Glu-C$_{(\beta)}$H$_2$, Pal-C$_{(\beta)}$H$_2$), 31.7 (several Pal-CH$_2$), 35.0 (triazolyl-C$_{(\beta)}$H$_2$, overlaps with solvent peak), 35.5 (Pal-C$_{(\alpha)}$H$_2$, overlaps with solvent peak), 38.3 (Lys-C$_{(\varepsilon)}$H$_2$), 38.8 (OEG-CH$_2$), 49.0 (OCH$_2$CH$_2$N), 49.0 (Ala-C$_{(\alpha)}$H), 50.4 (Ala-C$_{(\alpha)}$H), 53.4 (Glu-C$_{(\alpha)}$H), 53.5 (Glu-C$_{(\alpha)}$H), 54.1 (Lys-C$_{(\alpha)}$H), 55.6 (C-2), 59.3 (Val-C$_{(\alpha)}$H), 59.4 (Val-C$_{(\alpha)}$H), 66.3 (C-6), 67.7 (OCH$_2$CH$_2$N), 69.3 (OEG-CH$_2$), 69.8 (OEG-CH$_2$), 70.2 (OEG-C$_{(\alpha)}$H$_2$), 70.7 (OEG-CH$_2$), 70.9 (C-4), 74.4 (C-3), 75.2 (C-5), 101.6 (C-1), 123.1 (triazolyl-HCC$_{(\gamma)}$CH$_2$), 146.2 (triazolyl-HC$_{(\delta)}$CCH$_2$), 170.0 (CO), 170.7 (CO), 171.8 (CO), 172.3 (CO), 172.4 (CO), 172.6 (CO), 172.7 (CO), 173.9 (CO), 174.1 (CO), 174.2 (CO), 174.7 (2xCO), 174.8 (CO); ^{1}H-NMR (600 MHz, DMF-d$_7$): δ 0.86 (t, 3H, *J* = 7.0 Hz, Pal-CH$_3$), 0.91–0.95 (m, 12H, 4xVal-C$_{(\gamma)}$H$_3$), 1.22–1.30 (m, 20H, Pal-CH$_2$), 1.32–1.36 (m, 1H, Pal-CH$_2$), 1.39 (at, 6H, *J* = 7.3 Hz, 2xAla-C$_{(\beta)}$H$_3$), 1.43–1.53 (m, 3H, Lys-C$_{(\delta)}$H$_2$, Pal-CH$_2$), 1.54–1.62 (m, 2H, Pal-CH$_2$), 1.70–1.77 (m, 2H, Glu-C$_{(\beta)}$H$_2$), 1.82–1.87 (m, 2H, Pal-CH$_2$), 1.88 (s, 3H, acetyl-CH$_3$), 2.01–2.18 (m, 6H, Glu-C$_{(\beta)}$H$_2$, Lys-C$_{(\beta)}$H$_2$, 2xVal-C$_{(\beta)}$H), 2.27–2.35 (m, 2H, Pal-C$_{(\alpha)}$H$_2$), 2.38–2.51 (m, 6H, Glu-C$_{(\gamma)}$H$_2$, Lys-C$_{(\gamma)}$H$_2$, Glu-C$_{(\gamma)}$H$_2$), 2.59 (t, 2H, *J* = 7.8 Hz, triazolyl-C$_{(\beta)}$H$_2$), 2.93–2.97 (m, 2H, triazolyl-C$_{(\alpha)}$H$_2$), 3.20 (t, 2H, *J* = 7.0 Hz, Lys-C$_{(\varepsilon)}$H$_2$), 3.32–3.35 (m, 3H, H-4, OEG-CH$_2$), 3.46 – 3.48 (m, 2H, H-3, H-5), 3.50–3.53 (m, 2H, OEG-CH$_2$), 3.60–3.62 (m, 2H, OEG-CH$_2$), 3.64–3.66 (m, 2H, OEG-CH$_2$), 3.68 (dd, 1H, *J* = 8.5, 10.2 Hz, H-2), 3.92 (m, 1H, OCH$_2$CH$_2$N, overlaps with H$_2$O peak), 3.95 (s, 2H, OEG-C$_{(\alpha)}$H$_2$, overlaps with H$_2$O peak), 4.05 (dd, 1H, *J* = 6.2, 11.1 Hz, H-6b), 4.11 (dt, 1H, *J* = 4.4, 11.3 Hz, OCH$_2$CH$_2$N), 4.18 (d, 1H, *J* = 7.0 Hz, Val-C$_{(\alpha)}$H), 4.21 (d, 1H, *J* = 7.2 Hz, Val-C$_{(\alpha)}$H), 4.21–4.24 (m, 3H, Ala-C$_{(\alpha)}$H, Glu-C$_{(\alpha)}$H, Lys-C$_{(\alpha)}$H), 4.28 (dd, 1H, *J* = 1.8, 11.1 Hz, H-6a), 4.30–4.34 (m, 2H, Ala-C$_{(\alpha)}$H, Glu-C$_{(\alpha)}$H), 4.48 (d, 1H, *J* = 8.5 Hz, H-1), 4.56 (at, 2H, *J* = 5.1 Hz, OCH$_2$CH$_2$N), 7.87 (s, 1H, triazole-HC$_{(\delta)}$CCH$_2$); HRMS-ESI [M + H]: calcd for C$_{69}$H$_{120}$N$_{14}$O$_{25}$S, 1577.8348; found 1577.8343; [Cu]: 6.67 ng/mg.

GlcA PA (PA 3)—PA **3** was prepared by conjugating Alkyne PA and 2-azidoethyl β-D-glucuronoside (monosaccharide **3**)[54] using general procedure for Click-reaction. ATR-IR ν_{max}cm^{-1}: 3273 (strong, broad), 2919 (medium, broad), 2850 (medium), 1628 (strong), 1543 (strong), 1399 (medium, broad), 1227 (weak), 1112 (medium, broad), 1056 (medium, broad); ^{13}C-NMR (125 MHz, DMF-d$_7$): δ 13.4 (Pal-CH$_3$), 16.1 (Ala-C$_{(\beta)}$H$_3$), 17.3 (Ala-C$_{(\beta)}$H$_3$), 17.3 (Val-C$_{(\gamma)}$H$_3$), 17.3 (Val-C$_{(\gamma)}$H$_3$), 18.8 (Val-C$_{(\gamma)}$H$_3$), 18.9 (Val-C$_{(\gamma)}$H$_3$), 21.3 (triazolyl-C$_{(\alpha)}$H$_2$), 22.2 (Pal-CH$_2$), 23.2 (Pal-CH$_2$), 25.6 (Pal-CH$_2$), 26.9 (Glu-C$_{(\beta)}$H$_2$), 27.6 (Glu-C$_{(\beta)}$H$_2$), 28.6 (Lys-C$_{(\delta)}$H$_2$), 28.7–29.7 (several Pal-CH$_2$, overlaps with solvent peak), 30.4 (Val-C$_{(\beta)}$H), 30.6 (Val-C$_{(\beta)}$H), 30.6 (Lys-C$_{(\beta)}$H$_2$, Lys-C$_{(\gamma)}$H$_2$), 31.4 (Pal-CH$_2$), 34.6 (Glu-C$_{(\gamma)}$H$_2$), 34.8 (triazolyl-C$_{(\beta)}$H$_2$), 35.3 (Glu-C$_{(\gamma)}$H$_2$), 35.3 (Pal-C$_{(\alpha)}$H$_2$), 38.2 (Lys-C$_{(\varepsilon)}$H$_2$), 38.6 (OEG-CH$_2$), 48.4 (Ala-C$_{(\alpha)}$H), 49.8 (OCH$_2$CH$_2$N), 50.5 (Lys-C$_{(\alpha)}$H/Glu-C$_{(\alpha)}$H), 53.3 (Lys-C$_{(\alpha)}$H/Glu-C$_{(\alpha)}$H), 54.9 (Ala-C$_{(\alpha)}$H), 56.0 (Glu-C$_{(\alpha)}$H), 58.2 (Val-C$_{(\alpha)}$H), 58.4 (Val-C$_{(\alpha)}$H), 67.9 (OEG-C$_{(\alpha)}$H$_2$), 69.0 (OEG-CH$_2$), 69.5 (OEG-CH$_2$), 69.9 (OCH$_2$CH$_2$N), 70.3 (OEG-CH$_2$), 72.1 (C-4), 73.3 (C-2), 74.0 (C-5), 76.3 (C-3), 102.9 (C-1), 123.5 (triazolyl-HCC$_{(\gamma)}$CH$_2$), 146.0 (triazolyl-HC$_{(\delta)}$CCH$_2$), 170.3 (CO), 171.3 (CO), 172.0

(CO), 172.8 (CO), 172.9 (CO), 173.7 (CO), 173.8 (2xCO), 174.0 (CO), 174.9 (CO), 175.3 (CO), 178.3 (CO), 178.5 (CO); ^{1}H-NMR (600 MHz, DMF-d_7): δ 0.84 (t, 3H, *J* = 6.9 Hz, Pal-CH_3), 0.87–0.90 (m, 12H, Val-C$_{(\gamma)}H_3$), 1.20–1.28 (m, 22H, Pal-CH_2), 1.30–1.36 (m, 2H, Pal-CH_2), 1.38 (d, 3H, *J* = 7.2 Hz, Ala-C$_{(\beta)}H_3$), 1.41 (d, 3H, *J* = 7.1 Hz, Ala-C$_{(\beta)}H_3$), 1.44–1.58 (m, 2H, Lys-C$_{(\delta)}H_2$), 1.53–1.58 (m, 2H, Pal-CH_2), 1.74–1.81 (m, 2H, Lys-C$_{(\beta)}H_2$), 1.84–1.89 (m, 2H, Lys-C$_{(\gamma)}H_2$), 1.93–2.01 (m, 2H, Glu-C$_{(\beta)}H_2$), 2.06–2.13 (m, 4H, Glu-C$_{(\beta)}H_2$, Val-C$_{(\beta)}$H, Val-C$_{(\beta)}$H), 2.17–2.32 (m, 6H, Glu-C$_{(\gamma)}H_2$, Pal-C$_{(\alpha)}H_2$, Glu-C$_{(\gamma)}H_2$), 2.57 (t, 2H, *J* = 7.7 Hz, triazolyl-C$_{(\beta)}H_2$), 2.93–2.96 (m, 2H, triazolyl-C$_{(\alpha)}H_2$, overlaps with solvent peak), 3.17–3.22 (m, 3H, H-2, Lys-C$_{(\varepsilon)}H_2$), 3.31–3.43 (m, 4H, H-3, H-4, OEG-CH_2), 3.49–3.54 (m, 3H, H-5, OEG-CH_2), 3.61–3.62 (m, 2H, OEG-CH_2), 3.64–3.65 (m, 2H, OEG-CH_2), 3.69–4.04 (m, 3H, OCH_2CH_2N, Glu-C$_{(\alpha)}$H), 4.12 (t, 2H, *J* = 7.0 Hz, Glu-C$_{(\alpha)}$H), 4.15–4.20 (m, 2H, Lys-C$_{(\alpha)}$H, Ala-C$_{(\alpha)}$H), 4.27–4.30 (m, 2H, 2xVal-C$_{(\alpha)}$H, overlaps with H_2O), 4.27 (s, 2H, OEG-C$_{(\alpha)}$H), 4.37 (d, 1H, *J* = 7.8 Hz, H-1), 4.48 (q, 1H, *J* = 7.0 Hz, Ala-C$_{(\alpha)}$H), 4.59–4.65 (m, 2H, OCH_2CH_2N), 8.16 (s, 1H, triazole- HC$_{(\delta)}$CCH_2); HRMS-ESI [M + H]: calcd for $C_{67}H_{115}N_{13}O_{23}$, 1470.8307; found 1470.8284; [Cu]: 7.44 ng/mg.

GlcNAc PA (PA 4)—PA **4** was prepared by conjugating Alkyne PA and 2-Azidoethyl 2-acetamido-2-deoxy-β-D-glucopyranoside (monosaccharide **4**)[53] following general procedure for Click-reaction. ATR-IR ν_{max}cm^{-1}: 3273 (strong, broad), 2919 (medium), 2850 (weak), 1627 (strong), 1542 (strong), 1396 (medium, broad), 1226 (weak), 1075 (medium, broad), 1059 (medium, broad); ^{13}C-NMR (125 MHz, DMF-d_7: δ 13.7 (Pal-CH_3), 16.1 (Ala-C$_{(\beta)}H_3$), 17.9 (Ala-C$_{(\beta)}H_3$), 18.1 (2xVal-C$_{(\gamma)}H_3$), 19.2 (Val-C$_{(\gamma)}H_3$), 19.4 (Val-C$_{(\gamma)}H_3$), 21.7 (triazolyl-C$_{(\alpha)}H_2$), 22.5 (Pal-CH_2), 22.6 (acetyl-CH_3), 23.8 (Pal-CH_2), 25.9 (Pal-CH_2), 26.8 (Lys-C$_{(\beta)}H_2$), 27.8 (Glu-C$_{(\beta)}H_2$), 29.2 (Lys-C$_{(\delta)}H_2$), 29.3–29.8 (several Pal-CH_2, overlaps with solvent peak), 30.5 (Val-C$_{(\beta)}$H), 30.8 (Glu-C$_{(\beta)}H_2$), 30.9 (Pal-C$_{(\beta)}H_2$), 31.0 (Val-C$_{(\beta)}$H), 31.8 (Pal-CH_2), 34.6–35.9 (2xGlu-C$_{(\gamma)}H_2$, Lys-C$_{(\gamma)}H_2$, Pal-C$_{(\alpha)}H_2$), 35.1 (triazolyl-C$_{(\beta)}H_2$), 38.5 (Lys-C$_{(\varepsilon)}H_2$), 38.9 (OEG-CH_2), 48.6 (Ala-C$_{(\alpha)}$H), 49.9 (OCH_2CH_2N), 51.2 (Ala-C$_{(\alpha)}$H/Glu-C$_{(\alpha)}$H), 53.7 (Ala-C$_{(\alpha)}$H/Glu-C$_{(\alpha)}$H), 55.6 (Glu-C$_{(\alpha)}$H), 55.6 (C-2), 57.2 (Lys-C$_{(\alpha)}H_2$), 58.6 (Val-C$_{(\alpha)}$H), 58.9 (Val-C$_{(\alpha)}$H), 61.7 (C-6), 67.2 (OCH_2CH_2N), 69.5 (OEG-CH_2), 69.9 (OEG-CH_2), 70.3 (OEG-C$_{(\alpha)}H_2$), 70.6 (OEG-CH_2), 71.0 (C-4/C-5), 74.7 (C-3), 77.4 (C-4/C-5), 101.4 (C-1), 122.9 (triazolyl-HC$_{(\gamma)}$CH_2), 146.4 (triazolyl-HC$_{(\delta)}$CCH_2), 169.9 (CO), 170.8 (CO), 171.3 (CO), 172.1 (CO), 172.2, 172.7 (CO), 173.3 (CO), 173.8 (CO), 174.0 (CO), 175.0 (CO), 175.3 (CO),,177.8 (CO), 178.1 (CO); ^{1}H-NMR (600 MHz, DMF-d_7): δ 0.85 (t, 3H, *J* = 6.9 Hz, Pal-CH_3), 0.90 (at, 12H, *J* = 7.1 Hz, 4xVal-C$_{(\gamma)}H_3$), 1.22–1.37 (m, 20 H, Pal-CH_2), 1.40 (d, 3H, *J* = 7.1 Hz, Ala-C$_{(\beta)}H_3$), 1.45 (d, 3H, *J* = 7.0 Hz, Ala-C$_{(\beta)}H_3$), 1.48–1.59 (m, 6H, Lys-C$_{(\delta)}H_2$, 2xPal-CH_2), 1.78–1.85 (m, 2H, Glu-C$_{(\beta)}H_2$), 1.85–1.90 (m, 2H, Pal-C$_{(\beta)}H_2$), 1.90 (s, 3H, acetyl-CH_3), 1.94–1.97 (m, 2H, Lys-C$_{(\beta)}H_2$), 2.11–2.17 (m, 4H, Glu-C$_{(\beta)}H_2$, 2xVal-C$_{(\beta)}$H), 2.18–2.40 (m, 8H, Glu-C$_{(\gamma)}H_2$, Glu-C$_{(\gamma)}H_2$, Lys-C$_{(\gamma)}H_2$, Pal-C$_{(\beta)}H_2$), 2.95 (t, 2H, *J* = 7.9 Hz, triazolyl-C$_{(\beta)}H_2$), 2.75 (m, 2H, triazolyl-C$_{(\alpha)}H_2$, overlaps with solvent peak), 3.19–3.22 (m, 2H, Lys-C$_{(\varepsilon)}H_2$), 3.29–3.31 (m, 2H, H-4, H-5), 3.33–3.35 (m, 2H, OEG-CH_2), 3.50–3.52 (t, 2H, *J* = 5.7 Hz, OEG-CH_2), 3.54 (dd, 1H, *J* = 8.3, 10.1 Hz, H-3), 3.58–3.66 (m, 5H, H-6b, OEG-CH_2, OEG-CH_2), 3.70 (dd, 1H, *J* = 8.6, 10.1 Hz, H-2), 3.85 (m, 1H, H-6a, overlaps with H_2O peak), 3.88 (m, 1H, OCH_2CH_2N, overlaps with H_2O peak), 3.90 (m, 1H, Lys-C$_{(\alpha)}$H, overlaps with H_2O peak),

3.95 (s, 2H, OEG-$C_{(\alpha)}\underline{H}_2$), 4.06 (t, 1H, $J = 6.7$ Hz, Glu-$C_{(\alpha)}\underline{H}$), 4.13–4.18 (m, 3H, $OC\underline{H}_2CH_2N$, Glu-$C_{(\alpha)}\underline{H}$, Ala-$C_{(\alpha)}\underline{H}$), 4.31 (ad, 2H, $J = 7.3$ Hz, Val-$C_{(\alpha)}\underline{H}$), 4.48 (d, 1H, $J = 8.6$ Hz, H-1), 4.51–4.61 (m, 3H, $OCH_2C\underline{H}_2N$, Ala-$C_{(\alpha)}\underline{H}$), 7.84 (s, 1H, triazole-$\underline{H}C_{(\delta)}CCH_2$); HRMS-ESI [M + H]: calcd for $C_{69}H_{120}N_{14}O_{22}$, 1497.8780; found 1497.8777; [Cu]: 6.99 ng/mg.

Synthesis of other compounds

Details on synthesis, chemical modification, and characterization of other compounds (PA **5**, PA **6**, Alkyne PA, Cy3-PA, and Cy5-BMP-2) are provided in the Supplementary information in the online version of the paper.

Materials characterization, *in vitro*, and *in vivo* assays

Details on materials characterization (ICP-MS, TEM, SAXS, CD, zeta potential, SPR, confocal microscopy) and biological assays (C2C12 culture, ALP assay, RT-PCR, mineralization assay, Western blot, ELISA, BaF3-FR1C culture, anticoagulation assay, rat posterolateral lumbar intertransverse spinal fusion, μCT, histology, and statistical analysis) are provided in the Supplementary information in the online version of the paper.

Data availability

The data that support the findings of this study are available from the corresponding author upon reasonable request.

Supplementary Material

Refer to Web version on PubMed Central for supplementary material.

Acknowledgments

Funding was provided by the NIH National Institute of Dental and Craniofacial Research grant 5R01DE015920-10, and also the Louis A. Simpson & Kimberly Querrey Center for Regenerative Nanomedicine at Northwestern University. The SAXS experiments were performed at the DND-CAT located at Sector 5 of the Advanced Photon Source (APS). Synchrotron X-ray μCT experiments were performed at Sector 2-BM of the APS. We thank the following facilities at Northwestern University: Analytical BioNanotechnology Equipment Core, Peptide Synthesis Core, Center for Advanced Microscopy, Biological Imaging Facility, Keck Biophysics Facility, Integrated Molecular Structure Education and Research Center, Quantitative Bio-element Imaging Center, Center for Advanced Molecular Imaging, and Research Histology and Phenotyping Laboratory. The Biophysics Core Facility at University of Chicago was also used. Refer to SI for facilities support. S.S.L. thanks the Samsung Scholarship. We are grateful to S. Weigand for assistance with the X-ray scattering, D. Sebald (University of Würzburg, Germany) and A. Lander (University of California-Irvine, USA) for a generous gift of EHBMP-2, to D. Ornitz (Washington University, Saint Louis, USA) for providing the engineered BaF3 cell line, to L. Palmer and K. Sato for helpful discussions, to C. Haney for assisting with μCT scanning and analyses, and to M. Seniw for molecular graphics. Although not used in this manuscript, we also thank S. Pshenychnyi and Y. Goo in assisting us with recombinant protein production and proteomics.

References

1. Xu D, Esko JD. Demystifying heparan sulfate-protein interactions. Annu Rev Biochem. 2014; 83:129–157. [PubMed: 24606135]
2. Edwards IJ. Proteoglycans in prostate cancer. Nature Rev Urology. 2012; 9:196–206. [PubMed: 22349653]

3. Hudak JE, Bertozzi CR. Glycotherapy: new advances inspire a reemergence of glycans in medicine. Chem Biol. 2014; 21:16–37. [PubMed: 24269151]
4. Bramono DS, et al. Bone marrow-derived heparan sulfate potentiates the osteogenic activity of bone morphogenetic protein-2 (BMP-2). Bone. 2012; 50:954–964. [PubMed: 22227436]
5. Zhao B, et al. Heparin potentiates the in vivo ectopic bone formation induced by bone morphogenetic protein-2. J Biol Chem. 2006; 281:23246–23253. [PubMed: 16754660]
6. Sadir R, Imberty A, Baleux F, Lortat-Jacob H. Heparan sulfate/heparin oligosaccharides protect stromal cell-derived factor-1 (SDF-1)/CXCL12 against proteolysis induced by CD26/dipeptidyl peptidase IV. J Biol Chem. 2004; 279:43854–43860. [PubMed: 15292258]
7. Lortat-Jacob H, Baltzer F, Grimaud JA. Heparin decreases the blood clearance of interferon-gamma and increases its activity by limiting the processing of its carboxyl-terminal sequence. J Biol Chem. 1996; 271:16139–16143. [PubMed: 8663206]
8. Capila I, Linhardt RJ. Heparin-protein interactions. Angew Chem Int Ed. 2002; 41:391–412.
9. Perrimon N, Bernfield M. Specificities of heparan sulphate proteoglycans in developmental processes. Nature. 2000; 404:725–728. [PubMed: 10783877]
10. Li YC, et al. Interactions that influence the binding of synthetic heparan sulfate based disaccharides to fibroblast growth factor-2. ACS Chem Biol. 2014; 9:1712–1717. [PubMed: 24959968]
11. Ornitz DM, Leder P. Ligand specificity and heparin dependence of fibroblast growth factor receptors 1 and 3. J Biol Chem. 1992; 267:16305–16311. [PubMed: 1379594]
12. Murali S, et al. Affinity-selected heparan sulfate for bone repair. Biomaterials. 2013; 34:5594–5605. [PubMed: 23632323]
13. Lever R, Page CP. Novel drug development opportunities for heparin. Nature Rev Drug Discov. 2002; 1:140–148. [PubMed: 12120095]
14. Baskaran S, Grande D, Sun XL, Yayon A, Chaikof EL. Glycosaminoglycan-mimetic biomaterials. 3 Glycopolymers prepared from alkene-derivatized mono- and disaccharide-based glycomonomers. Bioconjug Chem. 2002; 13:1309–1313. [PubMed: 12440867]
15. Huang ML, Smith RA, Trieger GW, Godula K. Glycocalyx remodeling with proteoglycan mimetics promotes neural specification in embryonic stem cells. J Am Chem Soc. 2014; 136:10565–10568. [PubMed: 25019314]
16. Tyler PC, Guimond SE, Turnbull JE, Zubkova OV. Single-entity heparan sulfate glycomimetic clusters for therapeutic applications. Angew Chem Int Ed. 2015; 54:2718–2723.
17. de Paz JL, Noti C, Bohm F, Werner S, Seeberger PH. Potentiation of fibroblast growth factor activity by synthetic heparin oligosaccharide glycodendrimers. Chem Biol. 2007; 14:879–887. [PubMed: 17719487]
18. Hartgerink JD, Beniash E, Stupp SI. Self-assembly and mineralization of peptide-amphiphile nanofibers. Science. 2001; 294:1684–1688. [PubMed: 11721046]
19. Webber MJ, Appel EA, Meijer EW, Langer R. Supramolecular biomaterials. Nature Mater. 2015; 15:13–26.
20. Kiyonaka S, et al. Semi-wet peptide/protein array using supramolecular hydrogel. Nature Mater. 2004; 3:58–64. [PubMed: 14661016]
21. Müller MK, Brunsveld L. A supramolecular polymer as a self-assembling polyvalent scaffold. Angew Chem Int Ed. 2009; 48:2921–2924.
22. Ustun Yaylaci S, et al. Supramolecular GAG-like self-assembled glycopeptide nanofibers induce chondrogenesis and cartilage regeneration. Biomacromolecules. 2016; 17:679–689. [PubMed: 26716910]
23. Chabre YM, Roy R. Chem Soc Rev. 2013; 42:4657–4708. [PubMed: 23400414]
24. Rostovtsev VV, Green LG, Fokin VV, Sharpless KB. A stepwise huisgen cycloaddition process: copper(I)-catalyzed regioselective “ligation” of azides and terminal alkynes. Angew Chem Int Ed. 2002; 41:2596–2599.
25. Barceloux DG. Copper. J Toxicol Clin Toxicol. 1999; 37:217–230. [PubMed: 10382557]
26. Cui H, et al. Spontaneous and X-ray-triggered crystallization at long range in self-assembling filament networks. Science. 2010; 327:555–559. [PubMed: 20019248]

27. Ortony JH, et al. Internal dynamics of a supramolecular nanofibre. Nature Mater. 2014; 13:812–816. [PubMed: 24859643]
28. Newcomb CJ, et al. Cell death versus cell survival instructed by supramolecular cohesion of nanostructures. Nature Commun. 2014; 5:3321. [PubMed: 24531236]
29. Paine-Saunders S, Viviano BL, Economides AN, Saunders S. Heparan sulfate proteoglycans retain Noggin at the cell surface - A potential mechanism for shaping bone morphogenetic protein gradients. J Biol Chem. 2002; 277:2089–2096. [PubMed: 11706034]
30. Silva GA, et al. Selective differentiation of neural progenitor cells by high-epitope density nanofibers. Science. 2004; 303:1352–1355. [PubMed: 14739465]
31. Tantakitti F, et al. Energy landscapes and functions of supramolecular systems. Nature Mater. 2016; 15:469–476. [PubMed: 26779883]
32. Katagiri T, et al. Bone morphogenetic protein-2 converts the differentiation pathway of C2C12 myoblasts into the osteoblast lineage. J Cell Biol. 1994; 127:1755–1766. [PubMed: 7798324]
33. Lee SS, et al. Gel scaffolds of BMP-2-binding peptide amphiphile nanofibers for spinal arthrodesis. Adv Healthc Mater. 2015; 4:131–141. [PubMed: 24753455]
34. Van Teeffelen JW, Brands J, Stroes ES, Vink H. Endothelial glycocalyx: sweet shield of blood vessels. Trends Cardiovasc Med. 2007; 17:101–105. [PubMed: 17418372]
35. Fyrner T, et al. Saccharide-functionalized alkanethiols for fouling-resistant self-assembled monolayers: synthesis, monolayer properties, and antifouling behavior. Langmuir. 2011; 27:15034–15047. [PubMed: 22053781]
36. Bearinger JP, et al. Chemisorbed poly(propylene sulphide)-based copolymers resist biomolecular interactions. Nature Mater. 2003; 2:259–264. [PubMed: 12690400]
37. Ham HO, Park SH, Kurutz JW, Szleifer IG, Messersmith PB. Antifouling glycocalyx-mimetic peptoids. J Am Chem Soc. 2013; 135:13015–13022. [PubMed: 23919653]
38. Gandhi NS, Mancera RL. The structure of glycosaminoglycans and their interactions with proteins. Chem Biol Drug Des. 2008; 72:455–482. [PubMed: 19090915]
39. Ruppert R, Hoffmann E, Sebald W. Human bone morphogenetic protein 2 contains a heparin-binding site which modifies its biological activity. Eur J Biochem. 1996; 237:295–302. [PubMed: 8620887]
40. Kuo WJ, Digman MA, Lander AD. Heparan sulfate acts as a bone morphogenetic protein coreceptor by facilitating ligand-induced receptor hetero-oligomerization. Mol Biol Cell. 2010; 21:4028–4041. [PubMed: 20861306]
41. Groppe J, et al. Structural basis of BMP signalling inhibition by the cystine knot protein Noggin. Nature. 2002; 420:636–642. [PubMed: 12478285]
42. Bhandari M, et al. The effects of standard and low molecular weight heparin on bone nodule formation in vitro. Thromb Haemost. 1998; 80:413–417. [PubMed: 9759620]
43. Yu PB, et al. BMP type I receptor inhibition reduces heterotopic ossification. Nature Med. 2008; 14:1363–1369. [PubMed: 19029982]
44. Schlessinger J, et al. Crystal structure of a ternary FGF-FGFR-heparin complex reveals a dual role for heparin in FGFR binding and dimerization. Mole Cell. 2000; 6:743–750.
45. Eming SA, Martin P, Tomic-Canic M. Wound repair and regeneration: mechanisms, signaling, and translation. Sci Transl Med. 2014; 6:265sr266.
46. Jacques LB. Heparin: an old drug with a new paradigm. Science. 1979; 206:528–533. [PubMed: 386509]
47. Petitou M, van Boeckel CA. A synthetic antithrombin III binding pentasaccharide is now a drug! What comes next? Angew Chem Int Ed. 2004; 43:3118–3133.
48. Simmonds MC, et al. Safety and effectiveness of recombinant human bone morphogenetic protein-2 for spinal fusion: a meta-analysis of individual-participant data. Ann Intern Med. 2013; 158:877–889. [PubMed: 23778905]
49. Tovar JD, Claussen RC, Stupp SI. Probing the interior of peptide amphiphile supramolecular aggregates. J Am Chem Soc. 2005; 127:7337–7345. [PubMed: 15898782]
50. Webber MJ, Newcomb CJ, Bitton R, Stupp SI. Switching of self-assembly in a peptide nanostructure with a specific enzyme. Soft Matter. 2011; 7:9665–9672. [PubMed: 22408645]

51. Gottlieb HE, Kotlyar V, Nudelman A. NMR Chemical shifts of common laboratory solvents as trace impurities. J Org Chem. 1997; 62:7512–7515. [PubMed: 11671879]

52. Chen B, et al. Carbohydrate rod conjugates: ternary rod-coil molecules forming complex liquid crystal structures. J Am Chem Soc. 2005; 127:16578–16591. [PubMed: 16305247]

53. Eklind K, Gustafsson R, Tiden AK, Norberg T, Aberg PM. Large-scale synthesis of a Lewis B tetrasaccharide derivative, its acrylamide copolymer, and related di- and trisaccharides for use in adhesion inhibition studies with Helicobacter pylori. J Carbohyd Chem. 1996; 15:1161–1178.

54. Chernyak A, Kononov LO, Kochetkov NK. Synthesis of carbohydrate-amino acid conjugates related to the capsular antigen K54 from Escherichia coli O6:K54:H10 and artificial antigens therefrom. Carbohydr Res. 1991; 216:381–398. [PubMed: 1797387]

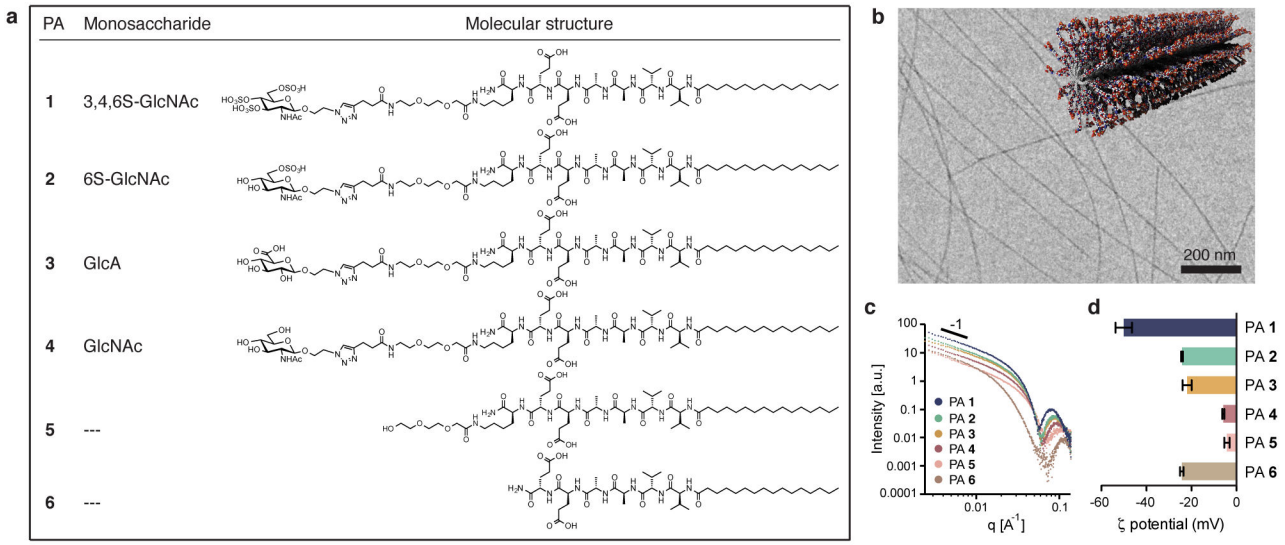

Figure 1. Design of supramolecular glycopeptide nanostructures

a, Chemical structures of PAs that are functionalized with a series of monosaccharides (**1–4**), oligo(ethylene glycol) (**5**), or not functionalized (**6**). **b**, Representative cryo-TEM image of filaments formed in 25 μM solutions of glycosylated PAs. Also shown is a molecular graphics representation of the glycosylated PA assembly. **c**, SAXS data showing the background subtracted scattered intensity versus the scattering vector q (log-log plot) for PAs **1–6** (6 mM) in saline. The data sets are offset vertically for clarity. **d**, Zeta potential measurements of solutions of PAs **1–6** (1 mM) in saline.

a

Proteins	# of amino acids	Heparin Binding Domain*
BMP-2	115	1 MQAKHKQRKR LKSSCKRH 18
BMP-4	106	1 KKNKNCRRH 9
FGF-1	141	113 KKNGSCKR GPRTHYGQK 129
FGF-2	154	128 RTG QYKLGSKTGP GQKA 144
VEGF	165	111 ARQENPCGPC SERRKHLFVQ DPQTCKCSCK NTDSRCKARQ LELNERTCRC DKPRR 165
Shh	176	10 G KRRHPKK 17
Noggin	206	106 GKKQR LSKKLRRKL 119

*See Supplementary References 1-7.

c

	Experimental K_D (M)	
Proteins	Heparin	PA 1
BMP-2	4.52 ± 0.77 e-8	3.15 ± 0.63 e-5
BMP-4	1.67 ± 0.14 e-8	1.01 ± 0.76 e-4
FGF-1	1.22 ± 0.19 e-7	1.28 ± 1.09 e-4
FGF-2	1.25 ± 0.11 e-9	8.55 ± 0.11 e-5
VEGF	4.75 ± 2.47 e-8	1.39 ± 0.35 e-4
Shh	4.49 ±1.23 e-8	-
Noggin	-	-

d

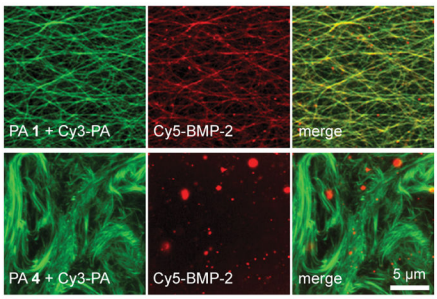

b

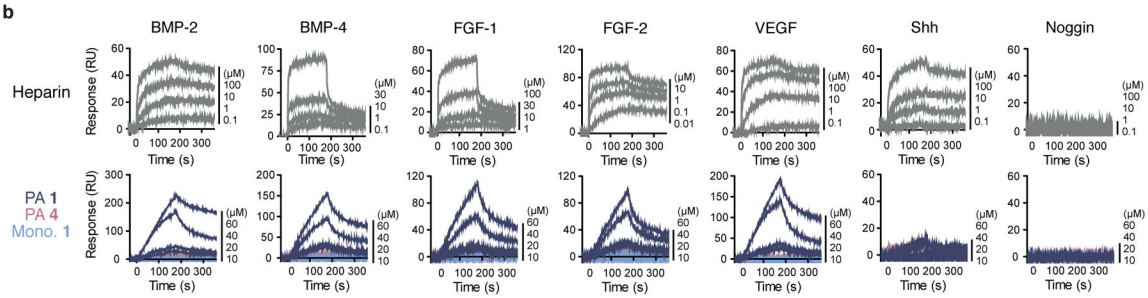

Figure 2. Supramolecular glycopeptide nanostructures bind heparin binding proteins

a, Table of seven proteins with their respective total number of amino acids and sequence of heparin binding domains. **b**, SPR sensorgrams showing binding response of heparin (top), and PA nanostructures or monosaccharide **1** (bottom) to immobilized proteins (RU: response units). **c.** Calculated equilibrium dissociation constants (K_D) from the SPR sensorgrams of heparin or PA **1** analytes to each protein. **d**, Confocal images of PA **1** (top) or PA **4** (bottom) nanostructures which are co-assembled with fluorescently labeled PA (Cy3-PA) (left), after mixing with Cy5-labeled BMP-2 (center). The merged images are also shown (right). **e**, [PA] = 6 mM, and [Cy5-BMP-2] = 5.2 μM.

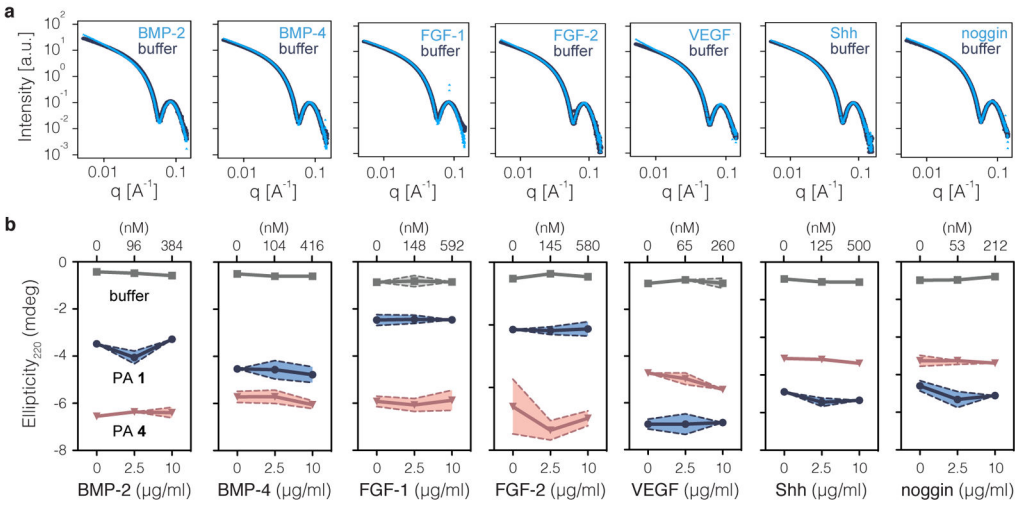

Figure 3. Structural stability of glycopeptide nanostructures following protein binding

a, SAXS data showing the background subtracted scattered intensity versus the scattering vector q (log-log plot) for PA **1** (6 mM) nanostructures mixed with blank buffer or with the following proteins at a concentration of 120 μg/mL: BMP-2 (4.6 μM), BMP-4 (5 μM), FGF-1 (7.1 μM), FGF-2 (6.9 μM), VEGF (3.1 μM), Shh (2.5 μM), and noggin (6 μM). **b**, CD ellipticity at 220 nm of blank buffer or PAs **1** and **4** (0.5 mM) in the absence or presence of seven proteins listed in **a**. For each PA, initial CD ellipticity values vary due to the presence of the appropriate amount of buffer (10.8% by vol.).

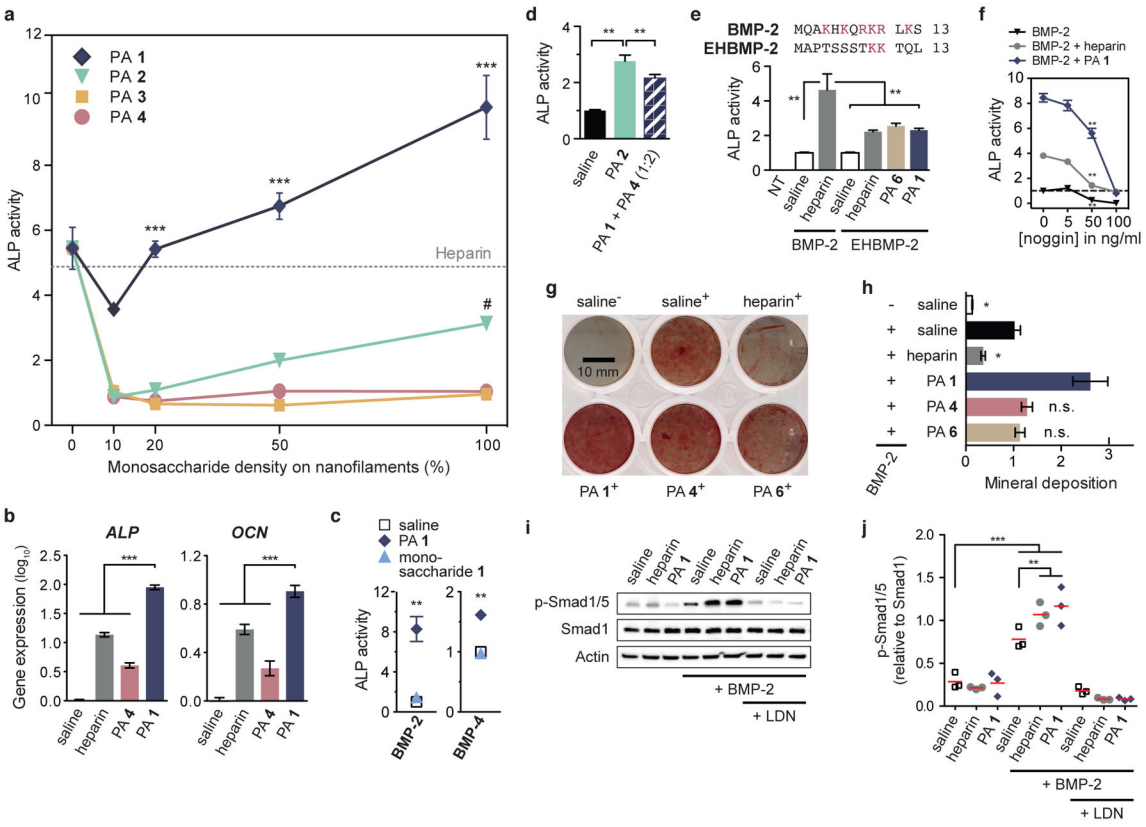

Figure 4. Effects of glycopeptide nanostructures on GF signaling *in vitro* in C2C12 cells

a, Plot of ALP activity in C2C12 cells treated with BMP-2 (75 ng/mL) and glycopeptide nanostructures (25 μM), as a function of increasing monosaccharide density on the nanostructures (treatment with heparin (0.62 μM or 10 μg/mL) is indicated by the dashed line). **b**, RT-PCR experiments evaluating ALP and OCN gene expression in the presence of BMP-2 (75 ng/mL) with identical treatments in **a. c**, BMP-2 (75 ng/mL) or BMP-4 (75 ng/mL) induced ALP activity following treatment with PA **1** nanostructures (25 μM) or monosaccharide **1** (25 μM). **d**, BMP-2 (75 ng/mL) induced ALP activity in C2C12 cells following treatment with either PA **2** alone or a co-assembly of PA **1** and PA **4** (1:2 molar ratio). In both systems, final [PA] = 25 μM. **e**, Bar graphs of ALP activity using wild-type BMP-2 (75 ng/mL) or a BMP-2 that has been mutated (EHBMP-2) (75 ng/mL) at the N-terminal heparin binding domain (in the protein sequence basic residues are colored in red). **f**, Effect of PA **1** nanofilaments (25 μM) or heparin (0.62 μM) on noggin inhibition of BMP-2 (75 ng/mL) activity (dashed line indicates the treatment of BMP-2 without noggin). **g.** Mineralization of C2C12 cells cultured with BMP-2 (100 ng/mL) in the presence of heparin (0.6 μM) or PA nanofibres (25 μM) (mineralization was visualized by Alizarin Red S staining and +/− indicates the presence/absence of BMP-2 in media). **h**. Quantitative analysis of Alizarin Red S stain in **g. i.** Western blot of C2C12 cells stimulated for 3 hr with BMP-2 (75 ng/mL), revealing the effect of heparin (0.6 μM) or PA **1** nanofibres (25 μM) on Smad phosphorylation. Cells were also treated with LDN-193189 (0.5 μM) to inhibit BMP-2 signaling. **j.** Quantification of immunoblotting shown in **h**. Data correspond to $n = 8$ with mean ± SEM (**a-f**, and **h)**, and $n = 3$ with mean indicated in red (**j**). For statistical analyses:

a, two-way analysis of variance (ANOVA) with Bonferroni post hoc test; ***$p < 0.001$ compared to PAs **2–4**, #$p < 0.05$ compared to PAs **3–4; b**, **d**, and **j**, one-way ANOVA with Newman-Keuls post hoc test, **$p < 0.01$, ***$p < 0.001$; **c**, **e**, **f** and **h**, Wilcoxon signed-rank test comparing medians to that of a control group, *$p < 0.05$ and **$p < 0.01$.

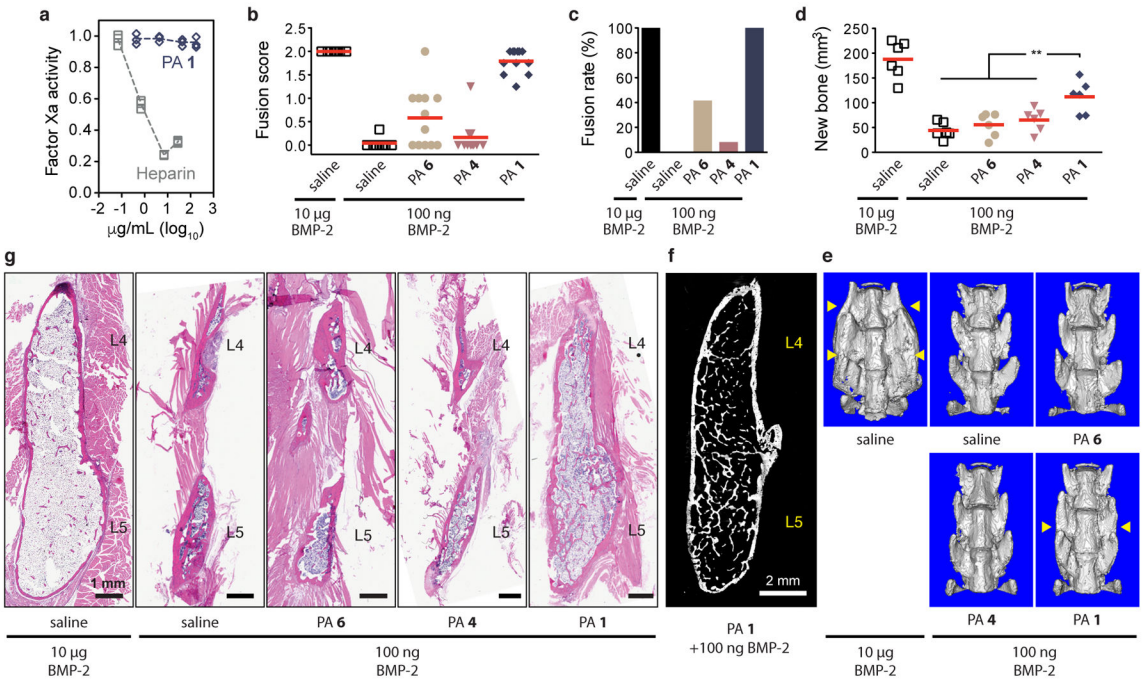

Figure 5. Glycopeptide nanostructures enhance bone formation

a, *In vitro* anticoagulation activity of heparin and PA **1**, evaluated by monitoring Factor Xa activity. **b–g**, Evaluation of the glycopeptide nanostructures in a rat spinal fusion model. Each animal was treated with a sub-therapeutic dose of 100 ng BMP-2 with saline or PA nanostructures. As a positive control, animals were treated with 10 μg BMP-2 with saline. **b**, Fusion scores from blind manual palpation analysis at 8-week post-op (0 = no fusion; 1 = unilateral fusion; 2 = bilateral fusion). **c**, Fusion rates of each treatment, in which fusion scores ≥ 1 are considered solidly fused. **d**, Comparison of fusion mass volume (mm^3) obtained from micro-computed tomography (μCT) analysis. **e**, Representative volume renderings from μCT (yellow arrows indicate fusion). **f**, Sagittal digital section through the fusion mass from an animal treated with 100 ng BMP-2 and PA **1** nanostructures (the volume rendering was obtained from high-resolution synchrotron X-ray μCT). **g**, Representative sagittal cross-sectional images of L4-L5 posterolateral spine specimens with H&E stain. Data are **a**, $n = 3$, center values as mean, **b**, $n = 8$ or 12, mean shown in red, and **d**, $n = 6$, mean shown in red. For statistical analysis, **b**, Wilcoxon signed-rank test, $^{**}p < 0.01$; **d**, one-way ANOVA with Newman-Keuls post hoc test, $^{**}p < 0.01$. **f** and **g**, Scale bar: 2 mm.